Nature Communications

https://doi.org/10.1038/s41467-026-69933-9

Article in Press

Complete defluorination of PFASs via photocatalytic reduction in water

Received: 19 June 2025

Accepted: 12 February 2026

Cite this article as: Chong, M., Zhou, Q., Xu, J. *et al.* Complete defluorination of PFASs via photocatalytic reduction in water. *Nat Commun* (2026). https://doi.org/10.1038/s41467-026-69933-9

MeiChi Chong, Qixin Zhou, Jingyi Xu, Zhaohui Wu, Enwei Zhu, Wenlu Li, Ling Zhang, Yan Guo & Yongfa Zhu

Complete defluorination of PFASs via photocatalytic reduction in water

MeiChi Chong [1], Qixin Zhou [1], Jingyi Xu [1], Zhaohui Wu [1], Enwei Zhu [1], Wenlu Li [1], Ling Zhang [1], Yan Guo [2]* and Yongfa Zhu [1]*

[1]Department of Chemistry, Tsinghua University, Beijing, China

[2]Department of Civil Engineering, The University of Hong Kong, Hong Kong, China

*E-mails: guoyan22@hku.hk, zhuyf@tsinghua.edu.cn

ABSTRACT:

The environmental persistence of per- and polyfluoroalkyl substances (PFASs), driven by the exceptional stability of their C–F bonds, presents a formidable challenge for remediation. Herein, we report the 5,10,15,20-tetraphenyl (4-aminophenyl) porphyrin (TAPP) aggregates as visible-light-driven photocatalysts capable of achieving almost-100% defluorination of PFASs without chemical additives. Central to this process is the ultra-stable TAPP radical species (TAPP•), which exhibits a lifetime exceeding 7 days under ambient conditions. Under visible-light irradiation, TAPP• generates reductive electrons with a potential of −2.68 V_{NHE}, enabling injection into the C–F antibonding orbitals to initiate defluorination. The exceptional stability of TAPP• arises from intramolecular charge delocalization mediated by the synergistic overlap between the lone-pair electrons distribution of the amino groups and the highest occupied molecular orbital. This work develops a steady radical strategy that leverages charge-delocalization to engineer photocatalysts with highly reductive electron, offering an approach to address persistent environmental contaminants.

Introduction

Per- and polyfluoroalkyl substances (PFASs) consist of fully or partially fluorinated alkyl chains, exhibiting daunting stability and bioaccumulation. PFASs pose significant environmental and health challenges due to their ubiquitous distribution and persistence. Thereinto, perfluorooctanoic acid (PFOA) and perfluorooctanesulfonic acid (PFOS) are the most prevalent PFASs found in numerous water sources[1]. In 2024, the World Health Organization cancer agency classified PFOA as carcinogenic to humans and PFOS as possibly carcinogenic[2]. Regulations on PFASs are gradually stricter, with latest drinking water quality standards (GB5749–2022) in China suggesting concentration limits of 40 ppt for PFOA and 80 ppt for PFOS, while the United States set compulsory maximum levels of 4.0 ppt for both. Water treatment facilities and fluorochemical industries face mounting pressure to comply with these restrictions.

The exceptional stability of PFAS arises from robust carbon-fluorine (C-F) bonds (bond energy: 536 kJ mol^{-1}) [3]and fluorine's high electronegativity. Together, these properties promote a stable, three-dimensional helical conformation (Fig. 1a). This structure creates a static electron shielding effect around the carbon atoms, effectively protecting the carbon chain from nucleophilic attack and rendering PFAS extremely refractory to remediation. To quantify the challenge, we calculated the total energy and relative energy of PFOS and its defluorinated counterpart. Based on these calculations (Supplementary Tables 1-2), the reduction potential for PFOS was inferred to be -2.37 V vs. NHE. This highly negative value indicates that strong reductants are essential for degradation. Furthermore, PFAS remediation faces dual challenges: (i) Ultra-low trace concentrations (often parts-per-trillion) hinder efficient enrichment from contaminated matrices, and (ii) inherent amphiphilicity drives conflicted environmental behavior - hydrophilic heads promote aqueous mobility while superhydrophobic perfluorinated chains strongly adsorb to solids, impeding both separation and degradation processes.

Current defluorination methods, such as sonolysis[4], advanced reduction processes[5] and thermal desorption[6, 7], are effective only for high PFAS concentrations. These methods necessitate auxiliary conditions, including high–energy inputs (electricity[8], sonication[9], UV[10, 11]) and additives (sulfite[12], iodide[13]) to enhance the generation of aqueous electrons (e_{aq}^-) and reactive species. Their high operational costs and stringent conditions hinder practical implementation. Consequently, the field prioritizes green remediation strategies capable of complete mineralization without toxic byproducts. While single-excitation photoredox catalysis fails to cleave robust C–F bonds in PFASs, tandem photoexcitation—leveraging two-photon absorption [14, 15]—has emerged to overcome the limited redox potential of visible-light photocatalysis. This approach enables solar-driven activation of recalcitrant bonds through consecutive photoexcitation. However, the nanosecond-scale lifetime of transient radicals necessitates abundant sacrificial reductants (e.g., γ-terpinene) to sustain electron flux for efficient defluorination[16].

Our laboratory has published many works highlighting that porphyrin-based supramolecular assemblies act as effective photocatalysts for H_2 evolution and CO_2 reduction[17-19], their photogenerated electrons lack the requisite reducing potential for C–F bond cleavage in PFAS. To overcome this limitation, we turned to a two-photon excitation strategy. Inspired by our previous success in manipulating localized hole orbitals in organic semiconductors to generate two-photon-driven carriers[20], we rationally tailored the frontier orbital energies and electronic structures of these porphyrin systems. This design enhances the generation of highly reducing electrons capable of driving demanding reductive transformations.

Benefiting from the past fundamental advantages, we address the challenging PFASs remediation through the rational design of TAPP supramolecular aggregates, which enable complete visible-light-driven PFAS defluorination without chemical additives. Density functional theory (DFT) and spectroscopic studies demonstrate that TAPP generates ultra-stable radical

species (TAPP$^{\bullet}$, lifetime >1 week) via synergistic overlap between the lone-pair electrons of its amino side chains and the porphyrin's highest occupied molecular orbital (HOMO). This stable TAPP$^{\bullet}$ enables consecutive photoexcitation to yield high-energy electrons (−2.68 V vs. NHE). Mechanistic investigations confirm direct electron injection into C–F antibonding orbitals, achieving quantitative defluorination of PFASs at environmentally relevant concentrations (0.1 ppm). Field trials in natural water systems and outdoor environments validate the catalyst's robustness under ambient conditions, establishing a scalable framework for mitigating PFAS contamination. This work advances a molecular engineering paradigm that integrates supramolecular charge delocalization with photocatalytic potency, offering a potential pathway to degrade recalcitrant pollutants.

Results and Discussion

Photoexcitation Produces Stable TAPP•

The proposed consecutive photoexcitation process for high-energy electron generated, as illustrated in Fig. 1b, operates through three critical stages: (1) Upon visible light irradiation, TAPP undergoes primary electron excitation from the highest unoccupied crystal orbital (HOCO) to the lowest unoccupied crystal orbital (LUCO). (2) Concomitant delocalization of lone-pair electrons from peripheral -NH_2 groups stabilizes the resulting TAPP radical species (TAPP•). (3) Continuous visible light irradiation triggering electron transition to higher-energy LUCO+1 orbital in TAPP• and generating an unprecedented reduction potential of -2.68 V vs NHE[20]. This potential surpasses the standard reduction threshold of PFOS (E_{red} = -2.37 V) by 310 mV, thermodynamically enabling direct C-F bond dissociation through single-electron transfer processes. Crystallographic, spectroscopic, and density functional theory (DFT) analyses collectively validate this mechanistic pathway.

To comprehensively validate the molecular structure and substituent integration, we employed a multi-technique spectroscopic approach. Vibrational spectroscopy provides chemical fingerprints: Fourier transform infrared spectroscopy (FTIR) analysis identifies characteristic N-H stretching modes at 3,300-3,500 cm^{-1}, with peak revealing distinct symmetric (3,420 cm^{-1}) and asymmetric (3,380 cm^{-1}) vibration components of the -NH_2 substituents (Supplementary Fig. 1a)[21]. X-ray photoelectron spectroscopy (XPS) depth profiling resolves the electronic environment of nitrogen species, where the N1*s* core-level spectrum (Supplementary Fig. 1b) exhibits two resolved components at 399.0 eV and 397.2 eV represent pyrrolic N and amine N, respectively. This multimodal structural verification establishes a robust foundation for subsequent electronic behavior analysis.

Ordered molecular assembly is essential to enhance exciton dissociation efficiency and facilitate rapid migration of photogenerated carriers to catalytic sites for efficient redox reactions with PFAS. [16] In TAPP, synergistic π-π and van der Waals interactions drive the formation of π-stacked aggregates. Powder X-ray diffraction (XRD) confirms the crystalline structure of TAPP aggregates (Fig. 1c). Pawley refinement determined the symmetry and lattice parameters (Supplementary Table 3), while DFT-optimized atomic coordinates resolved the molecular stacking configuration. We utilized spherical aberration-corrected cryogenic transmission electron microscopy (cryo-TEM) for crystalline structural analysis. The aggregates form uniform nanoparticles with catalytically active surfaces. Cryo-TEM lattice imaging resolved intersecting (1 4 $\bar{4}$) and (2 $\bar{1}$ $\bar{3}$) facets at an interplanar angle of 82°—consistent with the PXRD-refined crystal structure (Supplementary Fig. 2). Furthermore, we identified an ordered (0 0 2) stacking plane with a periodicity of 9.8 Å (corresponding to the molecular length of TAPP) and an interplanar spacing of 3.2 Å (Fig. 1d), directly visualizing π-π stacked TAPP assemblies. The concomitant suppression of photoluminescence (PL) emission indicates effective inhibition of electron-hole recombination within this ordered lattice (Supplementary Figs. 3-4). Photoelectrochemical measurements provide corroborating evidence: a 16-fold increase in photocurrent density and a 245% enhancement in surface photovoltage collectively demonstrate optimized carrier transport dynamics in the crystalline phase (Supplementary Fig. 3b-c). This phenomenon arises from periodic molecular stacking, which minimizes defect states and ensures unimpeded charge transfer to reactive centers.

The frontier molecular orbital architecture of TAPP dictates its photoexcited charge-transfer dynamics. As demonstrated in Supplementary Fig. 5, the HOMO, HOMO-2, and HOMO-3 orbitals localize predominantly on peripheral -NH_2 groups, while the lowest unoccupied molecular orbitals

(LUMO/LUMO+1) reside on the porphyrin macrocycle (Fig. 2a). This molecular orbital architecture determines hole accumulation on amino side chains and electron population within the polypyrrolic π-system under visible light excitation, inducing asymmetric charge separation. Time-dependent density functional theory (TDDFT) further revealed the influence of orbital distribution on electron-hole separation dynamics. The results show >85% hole density overlaps with nitrogen lone-pair orbitals (Fig. 2c, Supplementary Fig. 6), establishing robust spin-orbit coupling that enables lone-pair delocalization and stabilizes the TAPP$^{\bullet}$ radical. The persistence of this stabilized radical enables sequential secondary excitation to the high-energy TAPP$^{\bullet}$* state under low irradiance (non-laser light source), providing access to ultrahigh reduction potentials.

To elucidate the structure-dependent frontier orbital modulation in porphyrin systems, we engineered peripheral substituents with divergent electronic character: TAPP featuring strong electron-donating amino groups (-NH_2) was comparatively studied against tetra(4-cyanophenyl)porphyrin (TCyPP) bearing electron-withdrawing cyano groups (-CN) and benchmarked by unsubstituted tetraphenylporphyrin (TPP) as an electronic benchmark (Supplementary Figs. 7-8). This systematic design decouples substituent electronic effects from core porphyrin properties: -NH_2 groups lower orbital energy in peripheral sidechains via electron-donating conjugation, while -CN groups elevate orbital energy through electron-withdrawing conjugation.

FTIR validated the structural integrity of all porphyrin aggregates, confirming retention of functional group signatures after assembly (Supplementary Fig. 9). UV-vis spectroscopy further demonstrated broad visible-light harvesting capabilities (Supplementary Figs. 10-12). Crucially, a stark contrast emerges in frontier orbital distribution: whereas TAPP exhibits amino-dominated hole localization in its HOMO (Fig. 2b, Supplementary Fig.13), the cyano-functionalized analogue

TCyPP inverts this configuration—electron-withdrawing -CN groups dominate the lowest unoccupied orbitals (LUMO/LUMO+1). This electronic reversal precipitates directional electron transfer upon photoexcitation, with TD-DFT simulations demonstrating migration of electron density from pyrrolic nitrogen to peripheral cyano groups (Fig. 2c, Supplementary Fig. 14). Consequently, the constrained electron localization at cyano sites impedes lone-pair delocalization, thereby suppressing stable radical formation in TCyPP. This atomic-scale orbital engineering dictates divergent fates of peripheral lone-pair electrons: delocalization across the conjugated framework in TAPP versus localization within sidechains in TCyPP, directly modulating porphyrin radical generation efficiency.

Experimental validation through integrated electron paramagnetic resonance (EPR) and cyclic voltammetry confirms the exceptional radical stabilization capacity of TAPP. Transient sextet EPR signals in cyano-functionalized TCyPP and TPP decay completely within 3 minutes due to photobleaching (Supplementary Fig. 15), while TAPP exhibits persistent singlet-state resonance ($g = 2.007$) under visible light irradiation ($\lambda \geq 420$ nm, 100 mW cm^{-2}), confirming stable TAPP$^{\bullet}$ radical formation (Fig. 2d)[22]. In situ EPR kinetic analysis reveals rapid photogeneration ($\tau_{rise} = 16$ min) and slow decay ($\tau_{1/2} = 20$ min) of TAPP$^{\bullet}$ in solution, retaining 46% residual radical population after 30 minutes (Fig. 2e, Supplementary Figs. 16-17). To circumvent quenching of solution-phase TAPP$^{\bullet}$ by dissolved O_2 and H_2O, solid-state TAPP$^{\bullet}$ radicals were investigated. Their stability arises from crystallographic confinement effects, wherein π-π stacking interactions generate a protective lattice environment that spatially isolates unpaired electrons. The solid-state TAPP$^{\bullet}$ radical exhibits unprecedented environmental stability under ambient conditions (Fig. 2f). After undergoing 24-hour ambient diffuse light, the solid samples maintained their spin signal integrity with a remarkably low variance of ±5% in EPR intensity over an 8-day storage period in air (25°C, 40–60% relative humidity; Supplementary Fig. 18). Notably, this stability surpasses

conventional organic radicals (e.g., Mes-Acr$^{\bullet}$ typically quenches within 100 ps[14] and the lifetime of PDI$^{\bullet-}$ is 160 ps in solution[23]).

The exceptional kinetic persistence of the TAPP$^{\bullet}$ radical—maintaining 46% population after 30 minutes in solution and almost negligible attenuation over eight days in air—establishes the foundational platform for sequential photoactivation. Its prolonged lifetime enables continuous harvesting of visible photons ($\lambda \geqslant 420$ nm) during extended irradiation, while covalent *p*-π hybridization between amino groups and the porphyrin core localizes unpaired electrons at nitrogen sites, creating a metastable reservoir primed for secondary excitation. Electrochemical interrogation corroborates this resilience through two fully reversible single-electron transfers (–1.03 V and –1.45 V vs NHE, Supplementary Figs. 19-20)[24], confirming operational stability under aqueous redox cycling.

The absorption peaks of TAPP, TAPP$^{\bullet}$ and TAPP$^{\bullet}$* were identified by combining the experiment with TDDFT. Time-resolved spectral dynamics map the sequential charge-transfer cascade: attenuation of the Soret band (400–450 nm) signals ground-state depletion, followed by transient absorption at 450–650 nm marking TAPP$^{\bullet}$ accumulation, and culminating in a 764 nm signature of the high-energy TAPP$^{\bullet}$* state (Supplementary Fig. 21)[25]. Crucially, this three-stage trajectory (TAPP → TAPP$^{\bullet}$ → TAPP$^{\bullet}$*) emerges exclusively under visible-light irradiation, circumventing energy-intensive UV inputs. Thermodynamic validation via TD-DFT quantifies the TAPP$^{\bullet}$* excited-state reduction potential at –2.68 V vs NHE (Supplementary Notes 1-2), generating a 310 mV driving force relative to PFOS reduction (–2.37 V vs NHE). The synergy between TAPP$^{\bullet}$'s kinetic persistence ($\tau_{1/2}$ = 20 min) and TAPP$^{\bullet}$*'s thermodynamic superiority enables concerted C–F bond cleavage—achieving efficient defluorination unattainable with transient radical species.

Photocatalysis PFASs Defluorination

The photocatalytic defluorination mechanism of PFOS involves photoexcited electrons with sufficient energy from TAPP cleaving C-F bonds through consecutive photoexcitation processes. Systematic evaluation of TAPP's defluorination efficiency (deF%) was conducted under standardized conditions: 0.1 ppm PFAS concentration, 0.2 g L^{-1} catalyst loading, and additive-free aqueous systems. Prior to irradiation, adsorption equilibrium was established via 6-hour dark-phase preconditioning, with liquid chromatography-tandem mass spectrometry (LC-MS/MS) monitoring real-time PFOS concentrations. No significant desorption of PFOS was observed under irradiation.

TAPP aggregates exhibited exceptional adsorption capacity (Supplementary Fig. 22), achieving complete PFOS removal within 1 hour across a broad concentration range (0.1–50 ppm; Supplementary Fig. 23). Notably, no fluoride ions were detected in solution at this adsorption equilibrium stage. Subsequent irradiation with visible light ($\lambda \geqslant 420$ nm) triggered gradual fluoride ions accumulation(Supplementary Fig. 24). After 48 hours, fluoride release equivalent to the theoretical maximum from adsorbed PFOS was quantified (0.10 ± 0.01 ppm; Fig. 3a and Supplementary Figs. 25-26), confirming photocatalysis defluorination of PFOS contaminants over TAPP aggregates. Of noted, the IC analysis detected a peak corresponding to formate, which increased over time alongside fluorine ions. However, its concentration remained consistently below the method detection limit, preventing reliable quantification. In the absence of TAPP aggregates photocatalyst, PFOS exhibited negligible defluorination under identical experimental conditions, emphasizing that conventional photolytic processes (e.g. UV direct photolysis) are insufficient for PFOS degradation (Supplementary Fig. 27). The defluorination efficiency of PFOS showed negligible variation (<5% difference) when comparing visible-light ($\lambda \geq 420$ nm) and full-spectrum irradiation (300-800 nm) (Fig. 3b). This wavelength-independent behavior stems from

TAPP's narrow bandgap (1.25 eV) and broad spectral absorption, enabling efficient production of high energy electron across the visible spectrum (Supplementary Fig. 10).

The concentration dependence of PFOS levels (0.1–1 ppm) is shown in Fig. 3c, indicating defluorination decreases with increasing initial PFOS concentration. Comparative analysis of four representative PFAS compounds highlighted higher defluorination rates for perfluoroalkyl sulfonates (PFSAs: OBS, PFOS) versus perfluorocarboxylates (PFCAs: PFOA, PFdeA) (Fig. 3d). This superior PFSAs degradation efficiency contrasts markedly with conventional alkaline thermal treatment (NaOH/DMSO), which achieves >90% defluorination for PFOA in 24 h but less than 1% for PFOS in 150 h [26]. Additionally, while UVC photocatalysis achieves 25% defluorination for PFCAs like PFOA, they demonstrate $\leqslant$5% efficiency for PFSAs such as PFOS under anaerobic conditions[27] —a limitation rooted in the electron-withdrawing sulfonate group's capacity to stabilize radical intermediates. Remarkably, TAPP's consecutive photoexcitation mechanism overcomes this challenge, achieving 99.8% defluorination for both PFOS ($C_8F_{17}SO_3^-$) within 48 h through controlled reductive electron transfer (-2.68 V vs NHE). This efficacy originates from TAPP$^{\bullet-}$'s photogenerated electrons that bypass conventional oxidation bottlenecks, instead directly targeting the perfluoroalkyl chain's high-energy σ*(C-F) orbitals via electron injection. Cyclic experiments spanning 240 hours demonstrated TAPP's robust durability, maintaining >90% defluorination efficiency across five consecutive cycles (Fig. 3e). XRD (Supplementary Figs. 28-29) confirmed preserved crystallinity and structural integrity post-reaction, with no detectable phase transitions.

Reactive species identification through scavenging experiments (Fig. 3f) revealed electron-mediated C-F bond cleavage as the dominant pathway. Complete inhibition of defluorination (deF% <5%) by $AgNO_3$ unambiguously demonstrated photogenerated electrons' pivotal role, while isopropyl alcohol (IPA) showed partial inhibition (~22% efficiency loss), suggesting minor $^{\bullet}OH$

radical contribution. Methanol's negligible impact (<3% efficiency change) excluded holes as active participants, aligning with reported reductive degradation mechanisms for sulfonated PFAS.

TOF-SIMS detected no residual PFOS on the photocatalyst surface post-reaction (Supplementary Fig. 30). Furthermore, ^{19}F NMR investigations (Supplementary Fig. 31) shows that PFOS signal gradually decreased and disappeared with 48 h, confirming the defluorination of PFOS. Consistently, LC-MS/MS revealed no detectable PFOS signal in the post-reaction solution(Supplementary Figs 32-35). The terminal products of complete defluorination (Supplementary Fig. 32a-b) are identified as formate, oxalate, and lactate (quantified by HPLC and IC, Supplementary Fig.36), suggesting complete degradation through sequential defluorination and carbon chain cleavage[28]. Further analysis of PFOS degradation byproducts at the early-stage intermediates (~10% defluorination, Supplementary Fig. 37) revealed the presence of short-chain perfluorocarboxylic acids (e.g., $CF_3CH_2COO^-$) and fluorinated compounds (e.g., $CF_3CF_2CF_2CF_2CF{=}CF$, $CF_3CF_2CF_2^-$). The identification of intermediates with three or more carbons supports a direct defluorination mechanism, rather than conventional stepwise chain shortening mechanism[26, 29].

These findings demonstrate that TAPP's photogenerated electrons selectively engage with the high-energy σ*(C-F) orbitals of PFOS through direct electron injection. Based on the electronic configuration of PFOS, the reductive electrons predominantly populate the antibonding σ* orbital of its LUMO, which spans the perfluorinated carbon tail. This electron transfer destabilizes the molecular framework by elongating the C-C backbone, thereby unwinding PFOS's helical conformation and disrupting its static electrostatic shielding[30]. The increased internuclear distance between adjacent fluorine atoms weakens C-F bonds, facilitating their cleavage[31]. Mechanistic integration in Fig. 3g delineates the defluorination and mineralization process of PFOS.

Photoexcited Electrons from TAPP• Mediate C–F Cleavage

Operando XPS analysis reveals dynamic fluorine chemical state evolution during PFOS photodegradation. Upon TAPP adsorption, the F 1*s* binding energy exhibits a 0.60 eV downward shift (Supplementary Figs. 38-39), indicative of interfacial electron redistribution driven by electrostatic interactions between TAPP and PFOS. The interfacial charge characteristics of TAPP aggregates revealed a pronounced positive zeta potential of +48.7 in aqueous suspension (Supplementary Fig. 40), establishing strong electrostatic complementarity with anionic PFOS molecules. Real-time zeta potential monitoring during PFOS adsorption demonstrated rapid surface charge reversal: within 180 s of exposure to 10 ppm PFOS solution, the potential shifted from +50.1 mV to -9.3 mV. This dramatic charge inversion provides direct evidence of ultrafast PFAS adsorption, achieving sub-minute surficial accumulation.

Visible-light irradiation further reduces F 1*s* binding energy by 0.45 eV, corresponding to photoelectron injection into C–F bond.[32] Moreover, Hirshfeld surface analysis via the Independent Gradient Model based on Hirshfeld partition (IGMH) reveals critical non-covalent interactions governing TAPP-PFOS adsorption (Fig. 4a). Distinct electrostatic complementarity and H-bond emerges between PFOS's anionic sulfonic acid group ($-SO_3^-$) and TAPP's protonated amino moieties ($-NH_3^+$). Concurrently, the perfluorocarbon chain engages the porphyrin plane through extensive van der Waals contacts due to fluorine's enhanced polarizability. Significant atomic charge redistribution further corroborates wavefunction overlap between TAPP and PFOS, facilitating electron delocalization across the interface. [33] These results confirm an efficient electron transfer channel between TAPP and PFOS, which overcoming PFOS recalcitrance and enabling electron injection into C–F σ* orbitals. The robust interfacial interaction between TAPP aggregates and PFAS directs preferential electron transfer from photoexcited TAPP to PFAS over competing electron scavengers, as evidenced by EPR studies (Supplementary Fig. 41). While

superoxide anion radicals ($^{\bullet}O_2^-$) can form via oxygen reduction by TAPP-derived photoelectrons (a competing pathway reducing defluorination efficiency), EPR analysis revealed complete suppression of the characteristic DMPO-OOH adduct signal (indicative of $^{\bullet}O_2^-$ generation) upon introducing 1 ppm PFOS under identical irradiation conditions. This distinct signal disappearance quantitatively demonstrates PFOS's priority in capturing conduction-band electrons.

Femtosecond transient absorption spectroscopy (fs-TAS) delineates interfacial charge transfer dynamics in TAPP during PFOS defluorination. The transient absorption kinetics under 400 nm excitation (Fig. 4b and Supplementary Fig. 42) revealed two ground-state bleach (GSB) signals at 480 nm (Soret band) and 600 nm (Q band). [34] The long-lived stimulated emission (SE) peak at 670 nm indicated excited-state electron relaxation. Notably, short-lived excited-state absorption (ESA) at 760 nm is aligned with the persistent photoproduct absorption (PA) at 740 nm in UV-Vis-NIR spectra referring to second excited state (TAPP$^{\bullet}$*). The suppression of SE and ESA signals in the TAPP/PFOS system unequivocally underscores efficient interfacial electron transfer.

Triexponential fitting in Fig. 4c revealed three distinct phases—ultrafast phonon relaxation (τ_1 = 52.3 ps), excitation annihilation within the bandgap (τ_2 = 243.9 ps), and triplet-pair decay (τ_3 = 1852.3 ps). [35, 36] Further calculation shows that the average lifetime (τ_{ave}) is 1557.2 ps. Remarkably, the TAPP/PFOS system exhibited a drastically shortened lifetime τ_{ave} = 0.4 ps — a 99.97% reduction — providing definitive evidence of rapid charge transfer to PFOS. In summary, the mechanism of high-energy photoexcited electrons-driven C–F bond cleavage in PFOS proceeds through three key stages (Fig. 4d): (1) targeted adsorption via dual van der Waals and electrostatic interactions, (2) sequential electron excitation generating high-energy reductive states,

and (3) concerted reductive/oxidative degradation pathways achieving complete defluorination. This approach establishes a framework for designing advanced photocatalytic systems.

Environmental Suitability Assessment

The environmental adaptability of TAPP was systematically evaluated to bridge laboratory-scale efficiency with practical application requirements. A pilot-scale photocatalytic reactor (Fig. 5a), designed to mimic conventional wastewater treatment workflows, achieved complete (100%) PFOS defluorination within three days under natural solar irradiation, demonstrating its scalability under real-world conditions. To further assess interference from environmental matrices, three representative water systems were tested (Fig. 5b): municipal tap water (containing residual disinfectants and inorganic ions), natural organic matter (NOM, from Suwannee River), and soluble inorganic matter (IOM, 1 ppm K^+ and 10 ppm Na^+). Remarkably, TAPP retained full defluorination efficiency in NOM-laden systems, highlighting its robustness anti-interference to organic co-contaminants. For IOM and tap water matrices, however, complete defluorination required extended treatment durations (60 h), likely due to ionic competition from K^+/Na^+ reducing PFOS adsorption via electrostatic screening and the formation of electroneutral PFOS-cation complexes, which hindered interfacial congregation on TAPP's surface.

TAPP exhibits exceptional stability and energy efficiency, eliminating reliance on exogenous oxidants (e.g., peroxydisulfate) and artificial UV irradiation. As quantified in Fig. 5c and Supplementary Table 4, the solar-driven system reduces energy consumption by 90–98% relative to conventional photocatalysis. Comparative analysis reveals TAPP-mediated PFAS defluorination operates at 3.99 kW/m³, outperforming all reported light-activated catalytic systems. Notably, this represents >96% energy savings compared to technologies achieving $\geqslant 50\%$ defluorination efficiency. While CdS nanocrystals demonstrate near-complete defluorination, their prohibitive energy demand (139 kW m^{-3}) and cadmium toxicity preclude practical environmental deployment. The synergy of solar autonomy, chemical independence, ultra-low energy

requirements and non-toxic heavy metal properties of TAPP organic semiconductors establishes TAPP as a scalable, economical solution for PFAS remediation in resource-constrained settings.

In conclusion, the recalcitrant C-F bond cleavage constitutes the core challenge in PFAS remediation [41, 42]. Here, we engineer air-stable TAPP$^{\bullet}$ radicals (>7-day persistence) through molecular orbital synergy — where amino lone-pair electrons delocalize via π-conjugation/HOMO overlap upon photoexcitation. Subsequent photoactivation of these radicals generates highly reductive electrons (-2.68 V vs NHE) that selectively cleave C-F bonds in adsorbed PFOS via direct electron transfer. By achieving solar-powered defluorination without sacrificial reagents or energy-intensive infrastructure, this approach offers insights for sustainable PFAS destruction under ambient conditions. Furthermore, this study provided a feasible molecular engineering paradigm for generating high-energy photoexcited electrons, suggesting potential for demanding photocatalytic reductions such as hydrodehalogenation.

Methods

Chemicals and photocatalysts Synthesis

All the chemicals were AR grade and used as received. Heptadecafluorooctanesulfonic acid potassium salt (98%, PFOS-K) and sodium p-perfluorous nonenoxybenzene sulfonate (98%, OBS-Na) were purchased from J & K used as the source of pollutant PFOS and OBS, respectively. 13C4-PFOS were purchased from Wellington Laboratories (Guelph, Ontario, Canada), with concentration 50 μg ml^{-1} in methanol and was added to the sample to make a concentration of 0.05 ppm. PFOA and PFdeA was 98% from Meryer. 5,10,15,20-tetraphenyl (4-aminophenyl) porphyrin (98%, TAPP), tetraphenylporphyrin (98%, TPP) and meso-Tetra(4-cyanobenzyl) porphine(98%, TCyPP) was purchased from Bidepharm. Aluminum trichloride (99%) and methanol were purchased from Aladdin. Chloroform and dimethylformamide were both from Adams. NOM from Suwannee River (2R101N reference sample) was legally purchased from International Humic Substances Society (IHSS).

The synthesis of porphyrin derivatives was conducted through a straightforward method, in which TAPP (0.20 g, 0.15 mmol) was dissolved in $CHCl_3$/DMF (60 ml/15 ml) and methanol solution of $AlCl_3$ (0.07g, 5.5 mM). The mixture was refluxed at 80°C under nitrogen protection for 24 h and then rotary evaporated to concentrate. The residue solution was added dropwise into 100 ml DIW and aged for 1 h. The precipitation was centrifuged and washed with DIW several times to obtain purple powder (yield: 63%). TPP aggregates (yield: 70%) was obtained through a similar process without the addition of DMF and methanol, while TCyPP aggregates (yield: 65%) used DMF as the only solvent in the first step.

Characterisation and analytic methods

Powder XRD were obtained by Rigaku D/max-2400 X-ray diffractometer using a Cu Kα1 (λ= 1.5418 Å) at 40 kV and 200 mA. XPS spectrum was measured by ESCALAB 250Xi equipped

with an Al target. Cryo-electron microscopy (cryo-EM) were conducted by Thermo fisher Scientific Titan Krios with K_3 Summit Direct Electron Detector equipped with a GIF quantum energy filter. Fourier transform infrared (FT-IR) spectra were conducted by Bruker V70 FTIR spectrometer.

Water contact angle data was acquired from a DMe-211Plus of Kyowa Interface Science Co, Ltd. at ambient condition. UV-Vis diffuse reflectance spectroscopy was collected by Hitachi U-3010 spectrophotometer. The surface potential was evaluated through Zeta potential (Horiba SZ-100). For the adsorption kinetics, 0.02 g L^{-1} of sample was dispersed in 10 ppm PFOA solution (pH = 4.2) and 0.5 ml sample was collected at specific intervals of time. The photoluminescence (PL) spectra were collected on Edinburgh FS5 fluorescence spectrometer.

To further discover the photoelectrochemical properties of photocatalysts, a series of photoelectrochemical tests were conduct by CHI660E electrochemical workstation from Shanghai Chenhua instrument (Supplementary Fig. 43). The samples were evenly coated onto 2 × 4 cm ITO glass with concentration of 0.5 mg ml^{-1}. Pt wire was used as the work electrode and Ag/AgCl electrode as reference electrode. The photocurrent tests were excited by a 300 W xenon lamp and Mott-Schottky plots were resulted under the frequencies of 800, 1000 and 1200. The photoinduced radical were measured by electron paramagnetic resonance (CIQTEK EPR-100) with continues-wave X band frequency). Solid-state cyclic voltammograms of TAPP measured in tetrabutylammonium hexafluorophosphate ($TBAPF_6$)/DMSO with ferrocene/ferrocenium (Fc/Fc^+) redox couple as a reference voltammogram (scanning: 70 mV s^{-1}, WE: sample coated glassy carbon, RE: Ag/AgCl/KCl, CE: Pt wire).

Cryo-EM was employed under low-dose conditions to minimize electron-beam–induced damage and resolve the microscopic crystal structure. Measurements were conducted on a Thermo Fisher Scientific Titan Krios G3i microscope operated at 300 kV. An aqueous dispersion of TAPP

aggregates was dropped onto microgrids, vacuum-dried for 2 h, and subsequently frozen in liquid N_2 before transfer to the microscope using a cryogenic loader. Images were recorded in counting mode on a K3 Summit direct electron detector equipped with a GIF Quantum energy filter.

^{19}F NMR investigations were performed to study PFOS transformation. Samples were prepared in 90% aqueous sample solution and 10% D_2O (v/v) with D-trifluoroacetic acid as a chemical shift reference (-75.51 ppm), and 20% acetonitrile was additionally added to dissolve the photocatalyst and exclude adsorption effects for the photocatalytic samples. The ^{19}F NMR were acquired using a Bruker 600-MHz Avance NEO (AV-HD-600X) with a 5 mm triple resonance cryoprobe without proton decoupling, at a relaxation delay time of 8 s and 512 -1024 scans depending on the concentration.

Photocatalysis treatment

Photocatalytic degradation experiments were carried out in a 50 ml quartz tube containing PFASs aqueous solution, with a photocatalyst concentration of 0.2 g L^{-1} and no cocatalysts or additives. To ensure environmental relevance and practical applicability, the initial concentration was set at 0.1 ppm. A 500 W Xenon lamp, placed at the center of the water–cooling tube, is used as light source with light intensity of 70 mW cm^{-2}. For those experiments with visible light, a 420 nm filter was added (Supplementary Fig. 44). Each mixed suspension was stirred under dark conditions for 6 h to reach the adsorption equilibrium. For the outdoor experiment, 0.5 L 0.1 ppm PFOS with 0.2 g L^{-1}photocatalyst was filled in a reactor (Supplementary Fig. 45, size: 20 × 20 × 3 cm) and a pump was used to keep the internal recycling.

During fixed intervals of time, 2 ml samples were taken out and passed through 0.2 μm syringe filter to remove the solid for subsequent analysis. The degradation experiments were performed in triplicate and error bars represent to standard deviation. The fluorine ion and formate

were measured by ion chromatography (Metrohm 831, Switzerland) with a conductivity detector equipped with an A Supp 5 250/4.0 column, and sodium carbonate/sodium bicarbonate as mobile phase (Supplementary Figs. 46-47). Oxalate acid and lactic acid was measured by HPLC (Supplementary Figs. 48-49).

LC-MS/MS analyses were performed using Shimadzu LCMS-8060 triple Quadrupole MS (LC-MS/MS), coupled to Shim-pack GIST Phenyl-Hexyl (2 mm ID X 100 mm) (Supplementary Fig. 50-52). Detailed analytical procedures are described in Supplementary Note 3 and Supplementary Table 5. Time of flight secondary ion mass spectrometry (TOF–SIM, TOF SIMS 5–100, ION–TOF GmbH) equipped with Bi3+ ion beam was used to analyse the photocatalyst surface.

Theoretical calculations

The HOMO–LUMO analysis was performed using Gauss 16W. The states of structure and the vibration frequency calculations were carried out by the B3LYP functional and 6–31G(d) basis set, using water as an implicit solvent to simulate solution effects. All the atomic coordinates·of DFT calculation has been provided in Supplementary Data 1-3. Time–dependent density functional theory (TDDFT) was performed by the CAM–B3LYP/6–311G(d) to simulate the adsorption spectra. The PFOS adsorption of TAPP model was simulated, and the supercell of TAPP was illustrated by Material Studio programs. The final structure and total energy of STAPP–PFOS were optimized using Dmol3 module of Material Studio 2020[43, 44]. Multiwfn 3.7 program was used to analyze the adsorptive interaction of TAPP for PFOS and visualized through VMD 1.9.3 program[45, 46]

Data availability: The data that supports the findings of the study are included in the main text and supplementary information files. Source Data file has been deposited in Figshare under accession code https://doi.org/10.6084/m9.figshare.31169650.

Reference

1. Tang, Z.W., F. Shahul Hamid, I. Yusoff, and V. Chan, A review of PFAS research in Asia and occurrence of PFOA and PFOS in groundwater, surface water and coastal water in Asia. *Groundwater for Sustainable Development*. **22**, (2023).
2. Hong, J., et al., Environment relevant exposure of perfluorooctanoic acid accelerates the growth of hepatocellular carcinoma cells through mammalian target of rapamycin (mTOR) signal pathway. *Environ Pollut*. **341**: p. 122910, (2024).
3. Son, H., et al., The Adsorption Selectivity of Short and Long Per- and Polyfluoroalkyl Substances (PFASs) from Surface Water Using Powder-Activated Carbon. **12**(11): p. 3287, (2020).
4. Khoshyan, A., et al., Degradation of per-and poly-fluoroalkyl substances (PFAS) using ultrasonication: Effect of reactor materials. **63**: p. 105511, (2024).
5. Azarpira, H., et al., Photo-catalytic degradation of triclosan with UV/iodide/ZnO process: Performance, kinetic, degradation pathway, energy consumption and toxicology. *Journal of Photochemistry and Photobiology A: Chemistry*. **371**: p. 423-432, (2019).
6. Wang, J., et al., Thermal transformations of perfluorooctanoic acid (PFOA): Mechanisms, volatile organofluorine emissions, and implications to thermal regeneration of granular activated carbon. **479**: p. 135737, (2024).
7. Alinezhad, A., et al., Mechanistic investigations of thermal decomposition of perfluoroalkyl ether carboxylic acids and short-chain perfluoroalkyl carboxylic acids. **57**(23): p. 8796-8807, (2023).
8. Guan, Y., et al., Near-complete destruction of PFAS in aqueous film-forming foam by integrated photo-electrochemical processes. *Nature Water*. **2**(5): p. 443-452, (2024).
9. Xiong, X., et al., Complete defluorination of perfluorooctanoic acid (PFOA) by ultrasonic pyrolysis towards zero fluoro-pollution. **235**: p. 119829, (2023).
10. Chen, Z., et al., Enhanced UV photoreductive destruction of perfluorooctanoic acid in the presence of alcohols: Synergistic mechanism of hydroxyl radical quenching and solvent effect. *Applied Catalysis B: Environmental*. **316**, (2022).
11. Banayan Esfahani, E. and M. Mohseni, Fluence-based photo-reductive decomposition of PFAS using vacuum UV (VUV) irradiation: Effects of key parameters and decomposition mechanism. *Journal of Environmental Chemical Engineering*. **10**(1), (2022).
12. Gu, M., L. Liu, G. Yu, and J. Huang, Deeper Defluorination and Mineralization of a Novel PFECA (C7 HFPO-TA) in Vacuum UV/Sulfite: Unique Mechanism of H/OCF_3 Exchange. *Environ Sci Technol*. **57**(40): p. 15288-15297, (2023).

13. Chu, L., et al., Photo-Reductive Decomposition and Defluorination of Perfluorooctane Sulfonate (Pfos) in Uv/Iodide System. *SSRN Electronic Journal*. (2022).
14. MacKenzie, I.A., et al., Discovery and characterization of an acridine radical photoreductant. *Nature*. **580**(7801): p. 76-80, (2020).
15. Ghosh, I., T. Ghosh, J.I. Bardagi, and B. König, Reduction of aryl halides by consecutive visible light-induced electron transfer processes. *Science*. **346**(6210): p. 725-728, (2014).
16. Zhang, H., J.-X. Chen, J.-P. Qu, and Y.-B. Kang, Photocatalytic low-temperature defluorination of PFASs. *Nature*. **635**(8039): p. 610-617, (2024).
17. Jing, J., J. Yang, Z. Zhang, and Y. Zhu, Supramolecular Zinc Porphyrin Photocatalyst with Strong Reduction Ability and Robust Built-In Electric Field for Highly Efficient Hydrogen Production. *Advanced Energy Materials*. **11**(29), (2021).
18. Xu, J., et al., Efficient Photocatalytic Hydrogen and Oxygen Evolution by Side-Group Engineered Benzodiimidazole Oligomers with Strong Built-in Electric Fields and Short-Range Crystallinity. *Angew Chem Int Ed Engl*. **61**(45): p. e202212243, (2022).
19. Xu, J., et al., Guiding electron transfer for selective C_2H_6 photoproduction from CO_2. *Chem*. (2024).
20. Guo, Y., et al., Generation of holes from intra-valence band for enhanced oxidation potentials under visible light. *Chem*. **10**(4): p. 1252-1267, (2024).
21. Ma, X., et al., Pristine and carboxyl-functionalized tetraphenylethylene-based ladder networks for gas separation and volatile organic vapor adsorption. **3**(11): p. 15966-15974, (2018).
22. Tanaka, H., et al., π-Stacked Ion Pairs: Tightly Associated Charged Porphyrins in Ordered Arrangement Enabling Radical-Pair Formation. **144**(47): p. 21710-21718, (2022).
23. Zeman IV, C.J., S. Kim, F. Zhang, and K.S.J.J.o.t.A.C.S. Schanze, Direct observation of the reduction of aryl halides by a photoexcited perylene diimide radical anion. **142**(5): p. 2204-2207, (2020).
24. Gong, H.-X., et al., Photoexcited perylene diimide radical anions for the reduction of aryl halides: a bay-substituent effect. *Organic Chemistry Frontiers*. **5**(15): p. 2296-2302, (2018).
25. Rieth, A.J., et al., How Radical Are "Radical" Photocatalysts? A Closed-Shell Meisenheimer Complex Is Identified as a Super-Reducing Photoreagent. *J Am Chem Soc*. **143**(35): p. 14352-14359, (2021).
26. Trang, B., et al., Low-temperature mineralization of perfluorocarboxylic acids. *Science*. **377**(6608): p. 839-845, (2022).
27. Chowdhury, N., S. Prabakar, H.J.W.S. Choi, and Technology, Dependency of the photocatalytic and photochemical decomposition of per-and polyfluoroalkyl substances

(PFAS) on their chain lengths, functional groups, and structural properties. **84**(12): p. 3738-3754, (2021).

28. Patch, D., et al., Elucidating degradation mechanisms for a range of per- and polyfluoroalkyl substances (PFAS) via controlled irradiation studies. *Sci Total Environ*. **832**: p. 154941, (2022).
29. Zhang, Z., et al., Complete mineralization of perfluorooctanoic acid (PFOA) by gamma-irradiation in aqueous solution. *Sci Rep*. **4**: p. 7418, (2014).
30. Yang, H. and M.W. Wong, Application of Halogen Bonding to Organocatalysis: A Theoretical Perspective. **25**(5): p. 1045, (2020).
31. Jenness, G.R. and M.K.J.E.S.A. Shukla, What can Blyholder teach us about PFAS degradation on metal surfaces? **3**(3): p. 383-401, (2024).
32. Jung, M.-J., H.-R. Yu, and Y.-S.J.C.l. Lee, Preparation of fluorinated graphite with high fluorine content and high crystallinity. **26**: p. 112-116, (2018).
33. Gao, Q., et al., Facile preparation of multifunctional bamboo with superhydrophobic, conductive, and flame-retardant properties. *Industrial Crops and Products*. **188**, (2022).
34. Zhang, G., et al., Metal Complexes of the Porphyrin-Functionalized Polybenzoxazine. *Polymers*. **14**(3), (2022).
35. Yang, X., et al., Strong Interfacial Chemical Bonding in Regulating Electron Transfer and Stabilizing Catalytic Sites in a Metal-Semiconductor Schottky Junction for Enhanced Photocatalysis. *Small*. **20**(16), (2023).
36. Li, J., et al., Visible light-driven efficient palladium catalyst turnover in oxidative transformations within confined frameworks. *Nat Commun*. **13**(1): p. 928, (2022).
37. Le, T.X.H., H. Haflich, A.D. Shah, and B.P. Chaplin, Energy-Efficient Electrochemical Oxidation of Perfluoroalkyl Substances Using a Ti4O7 Reactive Electrochemical Membrane Anode. *Environmental Science & Technology Letters*. **6**(8): p. 504-510, (2019).
38. Luo, Y., et al., Investigating the effect of polarity reversal of the applied current on electrochemical degradation of per-and polyfluoroalkyl substances. *Journal of Cleaner Production*. **433**, (2023).
39. Gyaljen Tamang, S., G. Umlauf, J. Barz, and M.R. Ghomi, Degradation of PFOA solutions and PFAS-contaminated groundwater using atmospheric non-thermal plasma treatment. *Water Practice & Technology*. **19**(7): p. 2645-2654, (2024).
40. Mu, T., M. Park, and K.Y. Kim, Energy-efficient removal of PFOA and PFOS in water using electrocoagulation with an air-cathode. *Chemosphere*. **281**: p. 130956, (2021).
41. Jin, B., et al., In vivo generation of PFOA, PFOS, and other compounds from cationic and zwitterionic per-and polyfluoroalkyl substances in a terrestrial invertebrate (Lumbricus terrestris). **54**(12): p. 7378-7387, (2020).

42. Dasu, K., J. Liu, and L.S. Lee, Aerobic soil biodegradation of 8:2 fluorotelomer stearate monoester. *Environ Sci Technol*. **46**(7): p. 3831-6, (2012).
43. Delley, B., From molecules to solids with the DMol3 approach. *The Journal of Chemical Physics*. **113**(18): p. 7756-7764, (2000).
44. Delley, B.J.T.J.o.c.p., An all-electron numerical method for solving the local density functional for polyatomic molecules. **92**(1): p. 508-517, (1990).
45. Lu, T. and F. Chen, Multiwfn: A multifunctional wavefunction analyzer. **33**(5): p. 580-592, (2012).
46. Lu, T., A comprehensive electron wavefunction analysis toolbox for chemists, Multiwfn. *The Journal of Chemical Physics*. **161**(8), (2024).

Acknowledgments

This work was supported by the National Science Foundation of China (22136002), the National Key Research and Development Project of China (2020YFA0710304), and the Special Fund Project of Jiangsu Province for Scientific and Technological Innovation in Carbon Peaking and Carbon Neutrality (BK20220023). Y.G. is supported by an RGC Postdoctoral Fellowship from the Research Grants Council of the Hong Kong Special Administrative Region, China (PDFS2324-7S05).

We are grateful to Wenqing Yao, Jianxia Duan for their help with the XPS analysis; Zhanping Li and Chong Guo for TOF–SIMS; Yanfhai Jun and Wenyu Li for EPR and NMR; Qiang Han for LC-MS; Ruilong Zong, Chao Ma and Qin Li at the Analysis Center of Tsinghua University for assistance with TEM and XRD. We thank the drug metabolism department of the Center of Pharmaceutical Technology (Tsinghua University), especially Fang Wei and Guofang Tian, for their help with LC–MS/MS and IC.

We acknowledge the use of schematic icons designed by macrovector - Freepik.com under its Free License for use in Fig. 5a.

Author contributions

C.M.C. executed the study development and prepared writing–original draft. C.M.C. J.Y.X., Z.H.W. performed data analysis and interpretation. E.W.Z. and W.L.L. participated in experimental design. Q.X.Z. and L.Z performed DFT calculations. Y.G. and Y.F.Z. designed the study and supervised the manuscript. All authors read and edited the manuscript.

Competing interests

The authors declare no competing financial or non-financial interests.

Figure Legends

Fig. 1. Schematic Illustration of Visible-Light-Driven Photocatalytic Defluorination and Crystalline Validation. (a) Molecular configuration of PFOS highlighting perfluorinated alkyl chain and sulfonic acid group. (b) Photocarrier dynamics in TAPP aggregates: Visible-light-triggered ($\lambda \geq 420$ nm) electron generated and transfer pathways. Vis: Visible light. (c) Rietveld refinement of X-ray diffraction (XRD) and simulated unit cell and (d) spherical aberration corrected cryo-transmission electron microscopy (Cryo-TEM) image of TAPP aggregates.

Fig. 2. Photoexcitation Induced Stable TAPP$^{\bullet}$. DFT-calculated frontier molecular orbital distributions (HOMO±n, LUMO±n) for (a) TAPP and (b) TCyPP. (c) Hole–electron spatial mapping via TD-DFT/MESP isosurface analysis, identifying lone-pair delocalization domains critical for radical stabilization. (d) The EPR signal of TAPP$^{\bullet}$ under irradiation. Time-dependent evolution of double-integrated EPR signal intensity in (e) dichloromethane solution and (f) solid, demonstrating persistent TAPP$^{\bullet}$ lifetime.

Fig. 3. Photocatalysis PFASs Defluorination: Performance and Degradation Pathway. (a) Fluoride ion quantification via ion chromatography (IC) during visible-light-driven PFOS

degradation (0.1 ppm PFOS, visible light). (b) Comparative wavelength-dependent activity: Full-spectrum vs visible-light irradiation (0.1 ppm PFOS). (c) Concentration-dependent defluorination efficiency under full-spectrum illumination (PFOS: 0.1–1 ppm). (d) Substrate scope analysis of polyfluoroalkyl substances ([PFAS] = 0.1 ppm, catalyst loading = 0.2 g L^{-1}) (e) Long-term operational stability over 5 consecutive cycles (240 h total duration). (f) Reactive species identification through scavenger experiments (visible light, 25°C). (g) Proposed PFOS degradation pathway via sequential C–F bond cleavage and degradation. The yellow highlight represents LC-MS/MS detected products. Error bars represent the standard error of the mean from triplicate experiments and absent error bars fall within the symbols.

Fig. 4. High-Energy Photoexcited Electrons-Driven C–F Bond Cleavage in PFOS. (a) Molecular dynamics simulation and weak-interaction analysis of PFOS-adsorbed TAPP. *Top/Middle*: Independent Gradient Model based on Hirshfeld partition (IGMH) visualization of van der Waals interaction domains. *Bottom*: Differential atomic charge distribution ($\Delta\rho$) highlighting electron transfer regions. (b) Pseudocolor 2D map of femtosecond transient absorption spectroscopy (fs-TAS) under 400 nm excitation. (c) Triexponential kinetic decay profile at 640 nm, illustrating charge transfer dynamics. (d) Proposed sequential photoexcitation pathway: Single-electron transfer generates TAPP$^{\bullet}$ radicals, followed by second excitation to TAPP$^{\bullet}$* for direct electron injection into PFOS's antibonding σ*(C-F) orbitals.

Fig. 5. Comprehensive assessment of TAPP-mediated PFOS remediation under environmentally relevant conditions. (a) Integrated photocatalytic system demonstration: Process schematic and reactor configuration for TAPP-mediated PFOS defluorination, with outdoor sunlight-driven degradation performance (0.1 ppm initial concentration). (b) Influence of

co-existing constituents: Tap water, NOM, and IOM matrix. (c) Comparative analysis of photocatalytic PFAS remediation technologies: Efficiency and sustainability benchmarks. Energy consumption normalized per cubic meter treated (kWh/m^3) based on reported systems [37-40]. Error bars represent the standard error of the mean from triplicate experiments and absent error bars fall within the symbols.

Editorial Summary:

This study reports that visible-light-excited TAPP aggregates generate highly reductive electrons (−2.68 V vs NHE) to cleave PFAS C–F bonds without additives, enabling a sustainable strategy for practical PFAS remediation in contaminated water.

Peer Review Information: *Nature Communications* thanks Yang Yang, Naresh Kumar and Jun Sun for their contribution to the peer review of this work. [A peer review file is available.]

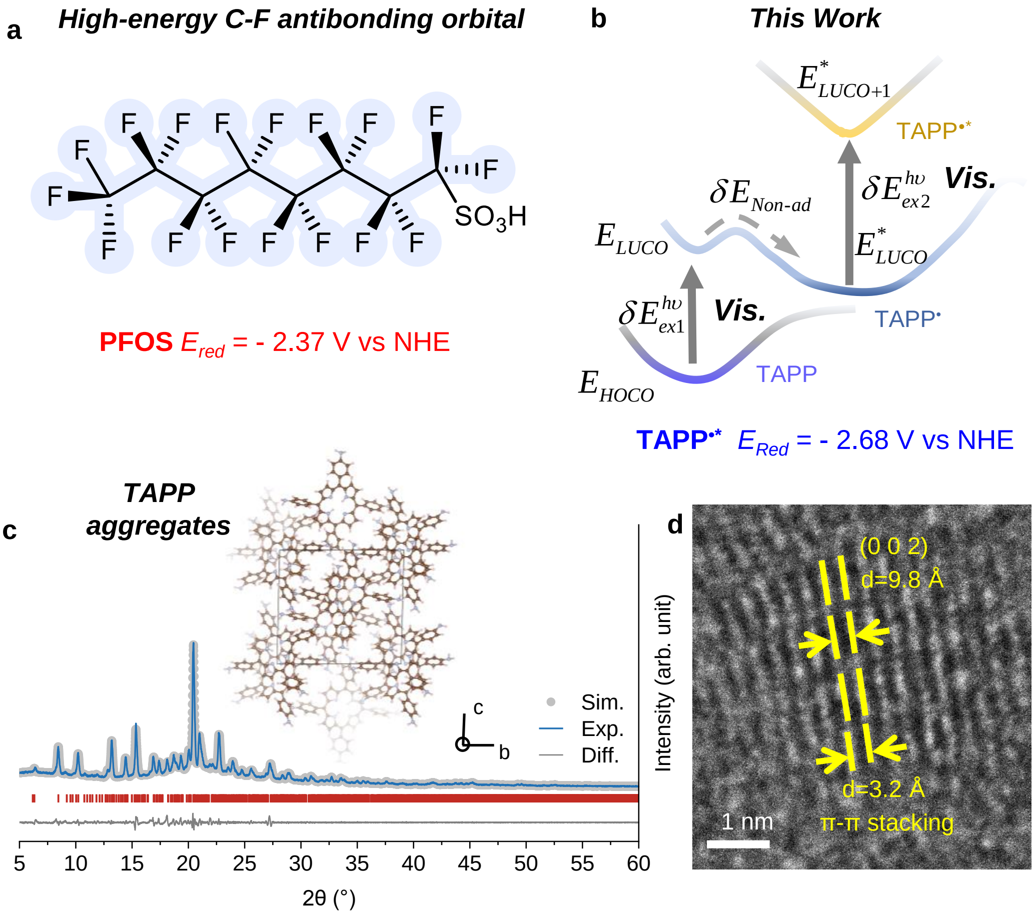
a
High-energy C-F antibonding orbital
F F F F F F F F F F F F F F F F F
SO3H
PFOS E_red = - 2.37 V vs NHE
b
This Work
E*_LUCO+1
TAPP•*
δE^hυ_ex2
Vis.
δE_Non-ad
E_LUCO
E*_LUCO
TAPP•
δE^hυ_ex1
Vis.
E_HOCO
TAPP
TAPP•* E_Red = - 2.68 V vs NHE
c
TAPP aggregates
c
b
Sim.
Exp.
Diff.
Intensity (arb. unit)
5 10 15 20 25 30 35 40 45 50 55 60
2θ (°)
d
(0 0 2)
d=9.8 Å
d=3.2 Å
π-π stacking
1 nm

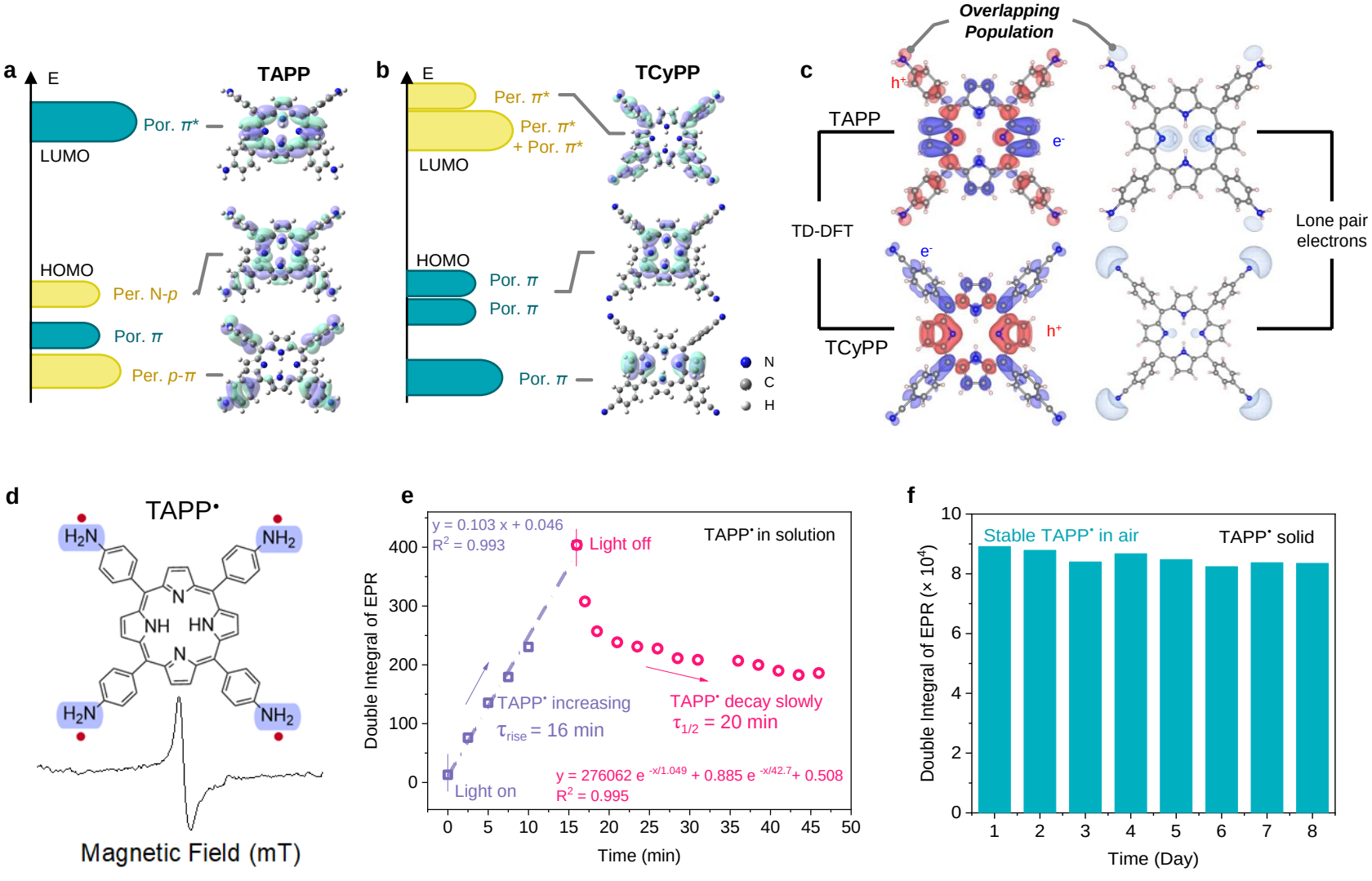
a
E
TAPP
Por. π*
LUMO
HOMO
Per. N-p
Por. π
Per. p-π
b
E
TCyPP
Per. π*
Per. π*
+ Por. π*
LUMO
HOMO
Por. π
Por. π
Por. π
N
C
H
c
Overlapping
Population
TAPP
TD-DFT
TCyPP
h+
e-
e-
h+
Lone pair
electrons
d
TAPP•
H2N
NH2
N
NH
HN
N
H2N
NH2
Magnetic Field (mT)
e
y = 0.103 x + 0.046
R2 = 0.993
Light off
TAPP• in solution
TAPP• increasing
τrise = 16 min
TAPP• decay slowly
τ1/2 = 20 min
Light on
y = 276062 e -x/1.049 + 0.885 e -x/42.7 + 0.508
R2 = 0.995
Double Integral of EPR
Time (min)
f
Stable TAPP• in air
TAPP• solid
Double Integral of EPR (× 10^4)
Time (Day)

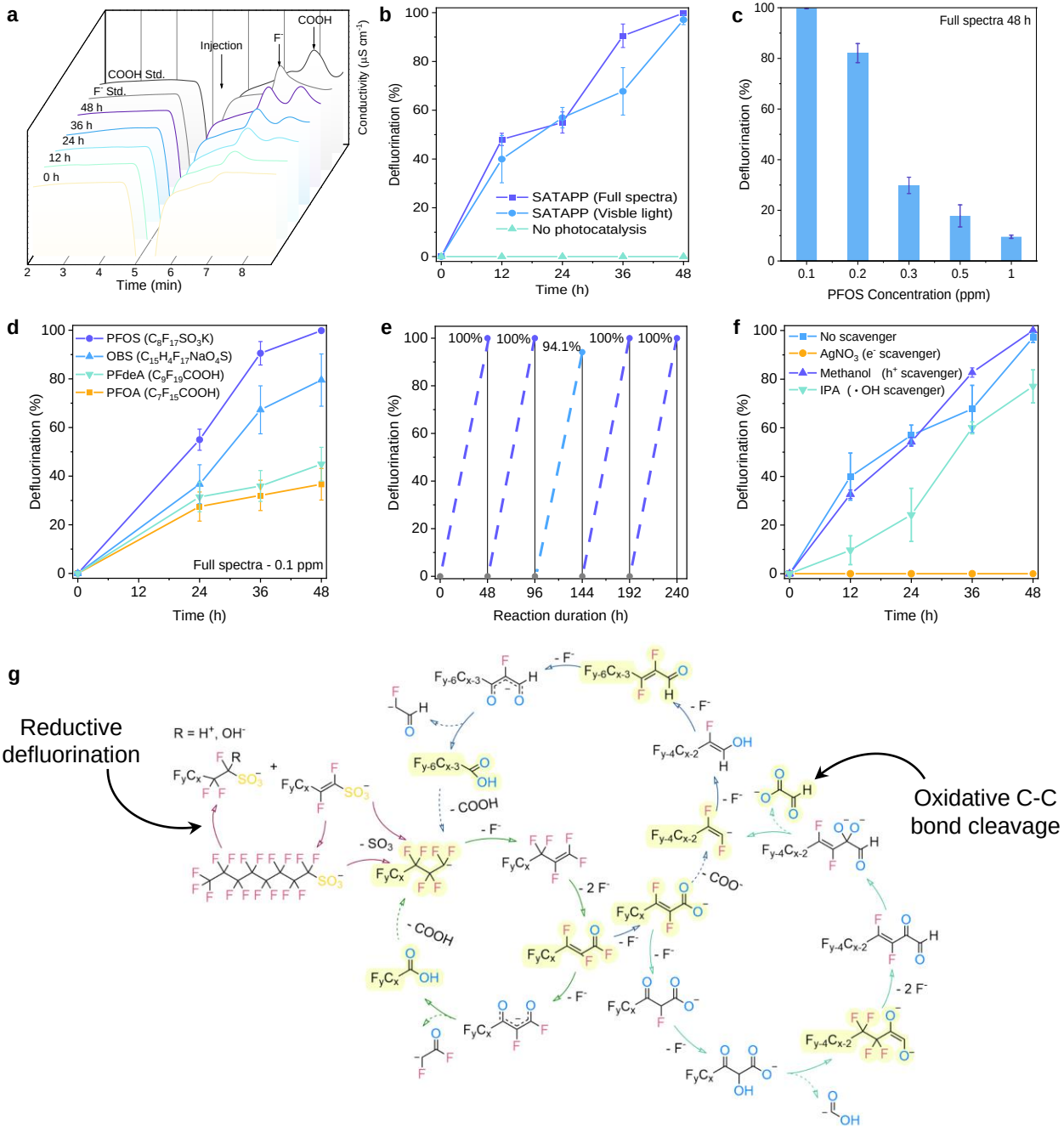
a
COOH
Injection
F⁻
COOH Std.
F⁻ Std.
48 h
36 h
24 h
12 h
0 h
Conductivity (μS cm⁻¹)
Time (min)
b
Defluorination (%)
SATAPP (Full spectra)
SATAPP (Visble light)
No photocatalysis
Time (h)
c
Full spectra 48 h
Defluorination (%)
PFOS Concentration (ppm)
d
PFOS (C8F17SO3K)
OBS (C15H4F17NaO4S)
PFdeA (C9F19COOH)
PFOA (C7F15COOH)
Full spectra - 0.1 ppm
Defluorination (%)
Time (h)
e
100%
100%
94.1%
100%
100%
Defluorination (%)
Reaction duration (h)
f
No scavenger
AgNO3 (e⁻ scavenger)
Methanol (h⁺ scavenger)
IPA (•OH scavenger)
Defluorination (%)
Time (h)
g
Reductive defluorination
R = H⁺, OH⁻
Oxidative C-C bond cleavage
- F⁻
- COOH
- SO3
- 2 F⁻
COO⁻

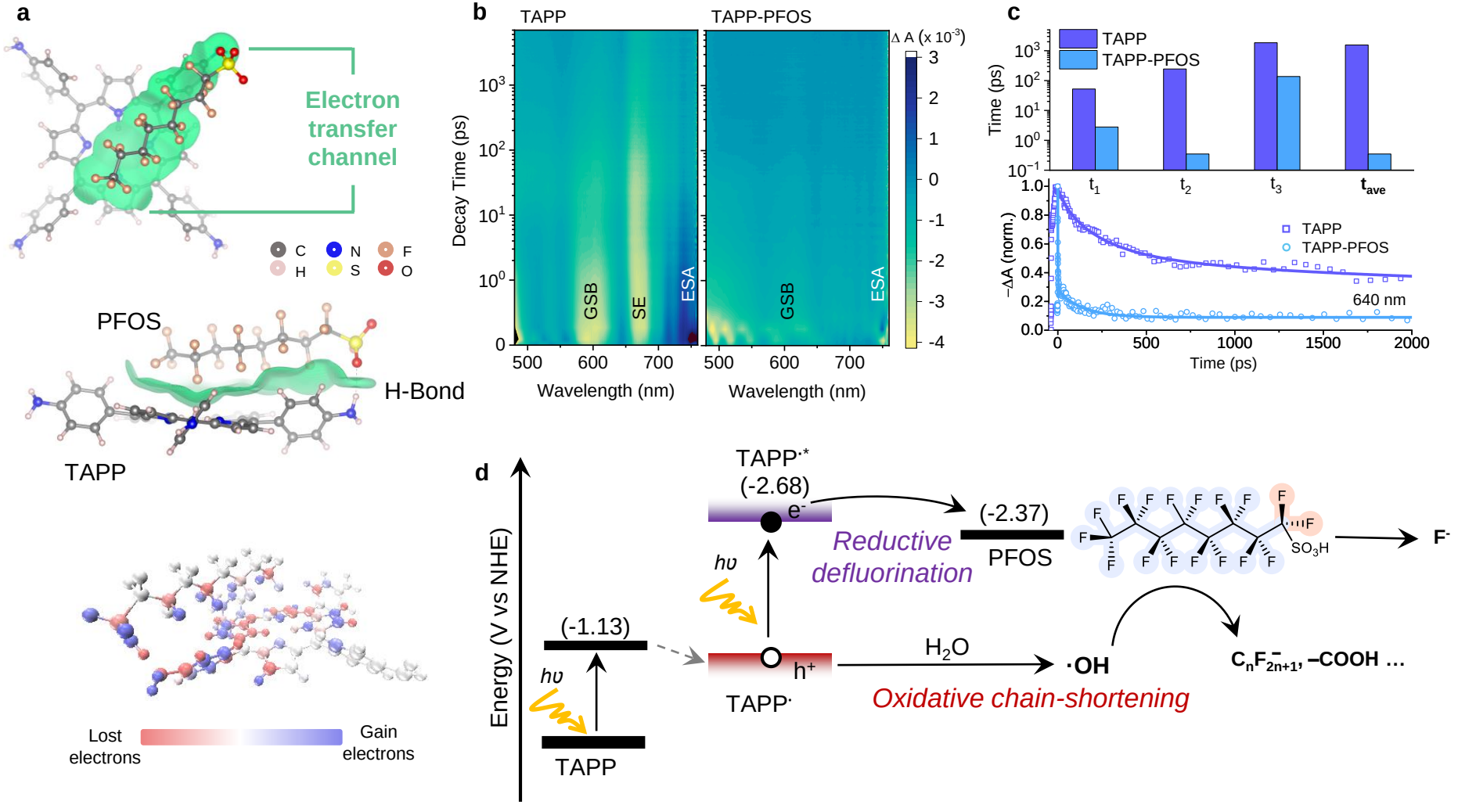
a
Electron transfer channel
C
H
N
S
F
O
PFOS
H-Bond
TAPP
Lost electrons
Gain electrons
b
TAPP
TAPP-PFOS
Δ A (x 10-3)
Decay Time (ps)
GSB
SE
ESA
Wavelength (nm)
c
TAPP
TAPP-PFOS
Time (ps)
t1
t2
t3
tave
−ΔA (norm.)
640 nm
d
Energy (V vs NHE)
TAPP·*
(-2.68)
e-
(-2.37)
PFOS
Reductive defluorination
F-
hυ
(-1.13)
h+
TAPP·
H2O
·OH
CnF2n+1–, –COOH …
Oxidative chain-shortening
TAPP

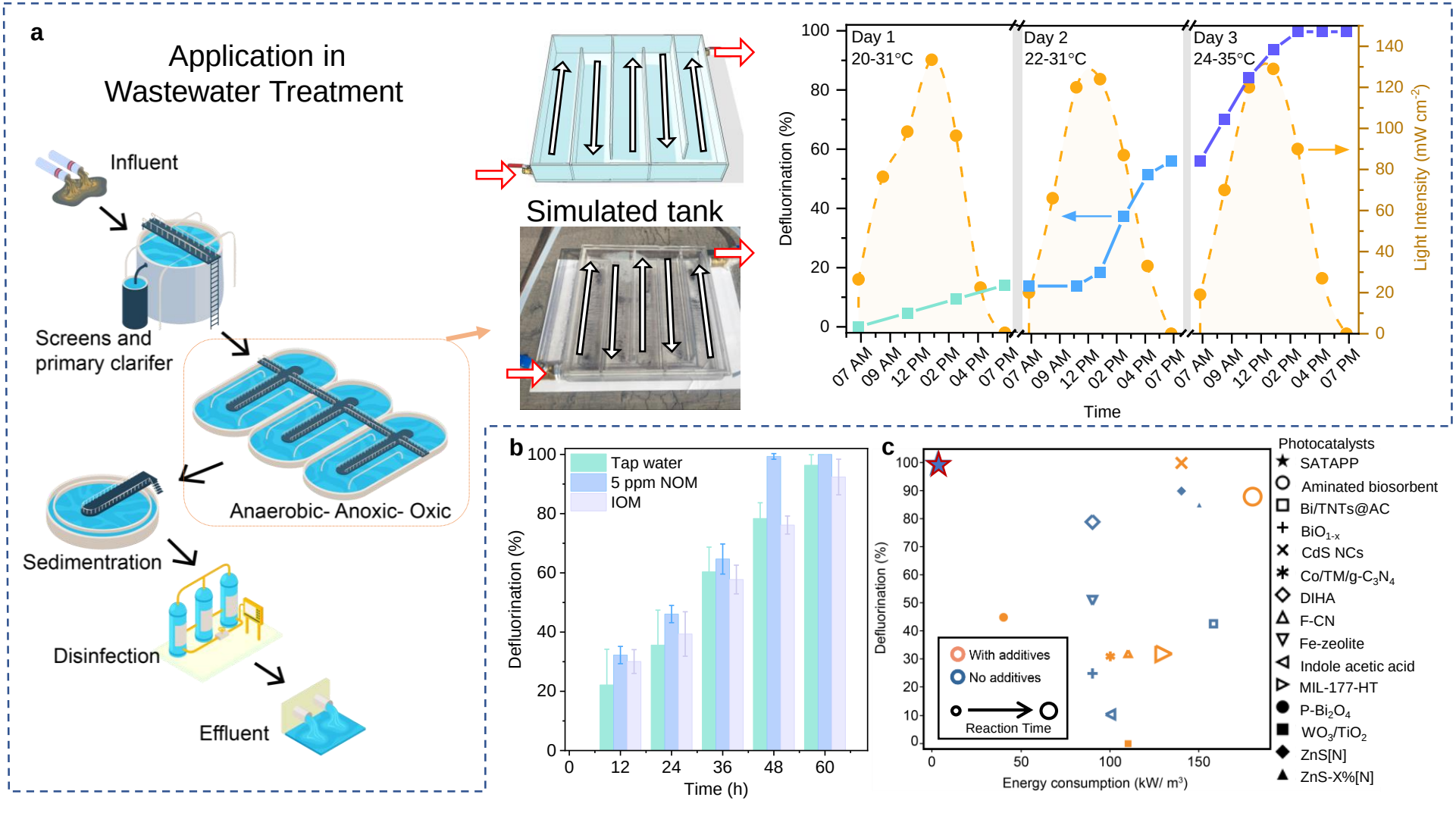
a
Application in
Wastewater Treatment
Influent
Screens and
primary clarifer
Anaerobic- Anoxic- Oxic
Sedimentration
Disinfection
Effluent
Simulated tank
Day 1
20-31°C
Day 2
22-31°C
Day 3
24-35°C
Defluorination (%)
Light Intensity (mW cm-2)
Time
07 AM
09 AM
12 PM
02 PM
04 PM
07 PM
b
Tap water
5 ppm NOM
IOM
Defluorination (%)
Time (h)
c
With additives
No additives
Reaction Time
Defluorination (%)
Energy consumption (kW/ m3)
Photocatalysts
SATAPP
Aminated biosorbent
Bi/TNTs@AC
BiO1-x
CdS NCs
Co/TM/g-C3N4
DIHA
F-CN
Fe-zeolite
Indole acetic acid
MIL-177-HT
P-Bi2O4
WO3/TiO2
ZnS[N]
ZnS-X%[N]